First Measurement of Differential Charged Current Quasielastic-like ν_μ–Argon Scattering Cross Sections In Kinematic Imbalance Variables With The MicroBooNE Detector

MICROBOONE-NOTE-1108-PUB

The MicroBooNE Collaboration
microboone_info@fnal.gov
May 27, 2022

ABSTRACT

We report the first measurement of flux-integrated multi-differential cross sections for charged-current events with muon neutrinos scattering on argon with solely a muon and a single proton in the final state as a function of kinematic imbalance variables. The measurement was carried out using the Booster Neutrino Beam at Fermi National Accelerator Laboratory within the MicroBooNE Liquid Argon Time Projection Chamber detector with an exposure of 6.79×10^{20} protons on target. Events were selected to enhance the contribution of charged-current mesonless interactions with one proton detected in the final state. The data discussed here are reported in terms of multi-differential cross sections in kinematic imbalance variables, which are generally sensitive to nuclear effects. The double-differential results in these variables can provide an excellent handle to disentagle specific nuclear aspects not easily isolated via single differential cross sections. Our results pave a path towards identifying regions of the phase-space where future interaction modeling development and Monte Carlo neutrino generator tuning efforts should concentrate.

EVENT SELECTION

Neutrino oscillation measurements aim to extract neutrino mixing angles, mass differences, the value of the charge-parity violating phase in the lepton sector, and to search for new physics beyond the Standard Model [1, 2]. For that to be achieved, an unprecedented understanding of neutrino-argon interactions is of utmost importance since a growing number of neutrino oscillation experiments employ Liquid Argon Time Projector Chamber (LArTPC) neutrino detectors [3–6]. The accuracy to which these experiments can extract neutrino oscillation parameters requires a good understanding of the neutrino energy. Experimentally, this energy is deduced from the measured kinetic energies of particles that are emitted following the neutrino interaction in the detector. The kinematic properties of such final-state particles reflect complex dynamics due to nuclear and initial-state effects of the interaction [7]. However, certain categories of nuclear effects can be isolated by variables built specifically to characterize the degeneracy between such effects [8–10].

This note reports cross sections in kinematic variables sensitive to nuclear effects using events with one detected muon with momentum $0.1 < p_\mu < 1.2\,\mathrm{GeV/c}$, and exactly one proton with $0.3 < p_p < 1\,\mathrm{GeV/c}$. This signal definition includes events with any number of protons below $300\,\mathrm{MeV}/c$, neutrons at any momenta, and charged pions with momentum lower than $70\,\mathrm{MeV}/c$. This choice is guided by the fact that their experimental signature of correlated muon-proton pairs is fairly straightforward to reconstruct [11–22]. Such events primarily originate from charged-current (CC) neutrino-nucleon quasielastic (QE) scattering interactions where the neutrino removes a single intact nucleon from the nucleus without producing any additional particles. This definition can also include contributions from interactions that lead to the production of additional particles that are absent from the final state due to nuclear effects, such as pion absorption, or have momenta that are below the experimental detection threshold.

The measurement used data from Runs 1-3 of the MicroBooNE detector [23], which is the first of a series of LArTPCs to be used for precision oscillation measurements [3, 6, 24]. The MicroBooNE detector has an active mass of 85 tonnes and is located along the Booster Neutrino Beam (BNB) at Fermilab, $463\,\mathrm{m}$ downstream from the target. The BNB energy spectrum extends to $2\,\mathrm{GeV}$ and peaks around $0.8\,\mathrm{GeV}$ [23].

A neutrino is detected by its interaction with an argon nucleus in the LArTPC. The secondary charged particles produced in the interaction travel through the liquid argon, leaving a trail of ionization electrons. These electrons drift horizontally and transverse to the neutrino beam direction due to the presence of an an electric field of $273\,\mathrm{V/cm}$, to a system of three anode wire planes located $2.56\,\mathrm{m}$ from the cathode plane.

The Pandora reconstruction package [25] is used to form individual particle tracks from the measured ionization signals. Under an assumption for the particle nature based on the energy deposition profile of the tracks, the measured track length for candidate protons [26] and muons [1] is used to obtain the kinetic energies and the momenta of the particles.

Thirty-two photomultiplier tubes (PMTs) are placed outside the TPC, facing the active volume, to collect argon scintillation light. Events are recorded if the PMT signals are in time-coincidence with the beam arrival time. A beam-off data sample is also acquired in the absence of the neutrino beam. At nominal running conditions, a neutrino interaction is expected in $\approx$ 600 BNB beam spills [27]. Trigger hardware and software selection cuts reject background events, mostly from cosmic muons. The process provides analysis samples that contain a neutrino interaction in $\approx$ 15% of the selected spills [28, 29]. The analysis presented here was performed on data collected from the BNB beam, with an exposure of 6.79×10^{20} protons on target (POT).

To avoid contributions from cosmic tracks and to minimize bin-migration effects, the selection considered only pairs of tracks with fully-contained muon and proton candidates in the fiducial volume of the MicroBooNE detector. The fiducial volume is defined by $10 < x < 246$ cm, $-105 < y < 105$ cm, and $10 < z < 1026$ cm. The x axis points along the negative drift direction with 0 placed at the anode plane, y points vertically upward with 0 at the center of the detector, and z points along the direction of the beam, with 0 at the upstream edge of the detector. Tracks are considered to be fully contained if both the start and end points are within this volume.

Muon-proton pair candidates were identified by requiring exactly two track-like objects and no shower-like ones based on a track-score variable from Pandora [30]. We used the log-likelihood ratio (LLR) score [31] to identify the muon and proton candidates. We significantly reduced the cosmic and non-CC1p0π contamination in our sample using the proton LLR and applied quality cuts to avoid flipped or broken tracks.

Neutrino interactions are simulated using the GENIE v3.0.6 event generator [32, 33]. The CC quasi-elastic (QE) and CC meson exchange current (MEC) neutrino interaction modes have been tuned to ν_μ-^{12}C CC0π data from T2K [34, 35]. GENIE generates all final state particles associated with the primary neutrino interaction and propagates the latter along the rescattering framework. The MC simulation contains beam-off data overlaid on top of simulated neutrino interactions to accurately describe the dominant cosmic backgrounds pertinent to surface detectors. For the simulated portion, the particle propagation is based on Geant4 [36], while the simulation of the MicroBooNE detector is performed in the LArSoft framework [37–39]. The beam-related MC backgrounds subtracted from the CC1p0π events are also simulated. Based on this MC, we estimate that our efficiency for selecting CC1p0π events is $\approx$ 10%, with a purity of $\approx$ 70%.

After the application of the event selection requirement, we retain 9051 CC1p0π candidate events in our data sample.

KINEMATIC IMBALANCE VARIABLES

Nuclear effects in CC neutrino-nucleus scattering can produce an imbalance between the initial neutrino momentum and the sum of final-state lepton and hadron momenta. In the case of the correlated muon-proton pair, the missing momentum in the plane transverse to the beam direction is defined as

$$\delta p_T = |\vec{p}_T{}^\mu + \vec{p}_T{}^p| \tag{1}$$

where $\vec{p}_T{}^\ell$ and $\vec{p}_T{}^p$ are, respectively, the projections of the momentum of the outgoing lepton and proton on the plane perpendicular to the neutrino direction. This variable, shown in figure 1a, encapsulates information related to the Fermi motion, but it is further smeared due to final state interactions (FSI) and multi-nucleon effects. The angular orientation of the transverse momentum imbalance ($\delta\alpha_T$) is obtained by

$$\delta\alpha_T = \arccos(\frac{-\vec{p}_T{}^\mu \cdot \delta\vec{p}_T}{p_T{}^\mu \cdot \delta p_T}), \tag{2}$$

and is shown in Fig. 1 (right). The variable would be uniformly distributed in the absence of any FSI due to the isotropic nature of the Fermi motion. In the presence of FSI, the proton momentum is on average reduced and the $\delta\alpha_T$ distribution becomes asymmetric with most of the events located in the 180° region. Typical sources of FSI leading to these asymmetric effect would be hadron/pion production or absorption, charge exchange, and (in)elastic scattering [40].
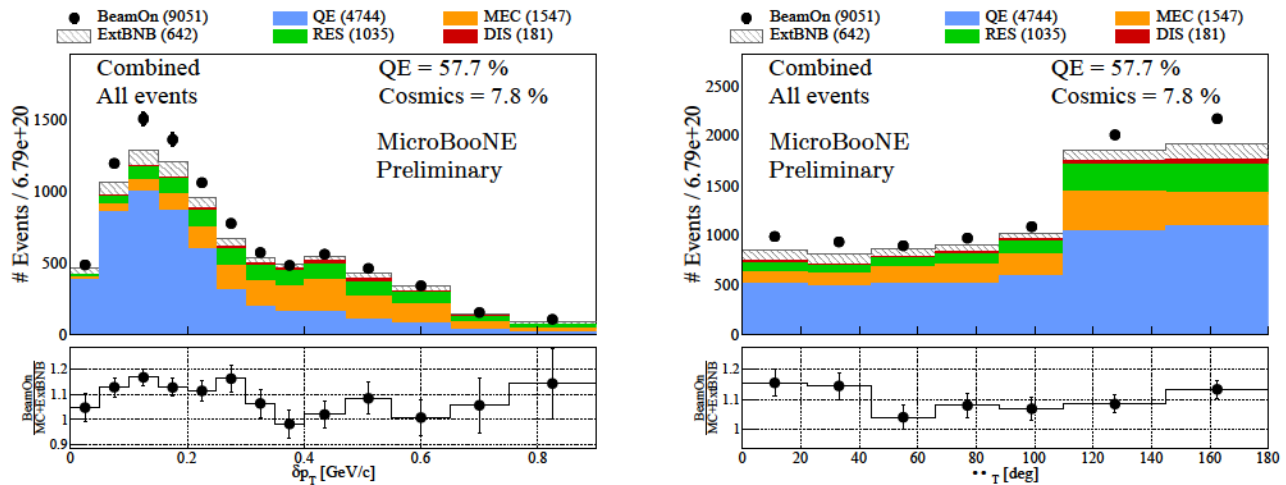
FIG. 1. Interaction breakdown of the CC1p0π events as a function of δp_T (left) and $\delta\alpha_T$ (right) into quasi-elastic (QE), meson exchange currents (MEC), resonance (RES), and deep inelastic scattering (DIS) events. ExtBNB refers to the cosmics acquired in the absence of the neutrino beam.

The muon-proton momentum imbalances parallel and transverse to $\delta\vec{p}_T$ [41] provide further handles over the Fermi motion and the FSI processes, respectively. The corresponding variables are defined as

$$\delta p_{Tx} = (\hat{p}_\nu \times \hat{p}_T^\mu) \cdot \delta\vec{p}_T$$
$$\delta p_{Ty} = -\hat{p}_T^\mu \cdot \delta\vec{p}_T, \tag{3}$$

and, in terms of the magnitudes,

$$\delta p_{Tx} = \delta p_T \cdot \sin\delta\alpha_T$$
$$\delta p_{Ty} = \delta p_T \cdot \cos\delta\alpha_T. \tag{4}$$

Fig. 2 (left) shows the measured event rates in δp_{Tx}. Interactions on free nucleons would produce a delta function at $0\,\text{GeV/c}$, because the muon and proton final states must balance. The QE peak is centered around $0\,\text{GeV/c}$ and its width mostly results from the Fermi motion. If we assume no significant deviation in the non-QE distributions originating from MEC and RES/DIS events, then data-MC discrepancies could imply an mismodeling of the argon Fermi motion in the argon nucleus, and/or a difference in the total fraction of the FSI contribution.

Unlike the δp_{Tx} distribution, we observed a non-QE tail towards the negative δp_{Ty} values shown in figure 2a. Inelastic events such as MEC, resonance, and DIS transfer a small fraction of the lepton momentum to the final state proton, since multiple final state particles are often involved. Therefore, the protons tagged in the non-QE events will on average have less momenta then the muons and the $\delta p_{T,y}$ distribution is shifted to the left.

CROSS-SECTION EXTRACTION TECHNIQUE AND SYSTEMATICS

We reported the extracted cross sections using the Wiener Single Value Decomposition (Wiener-SVD) unfolding technique as a function of true kinematic variables [42]. Unfolding corrects a measured event rate defined in Eqn. 5 for inefficiency and resolution effects. This is achieved by performing a minimization of a χ^2 score that compares data to a true prediction and allows for a regularization term. A Wiener filter determines the level of regularization that is required to minimize the mean square error between the variance and bias of the result. Apart from the measured event rate, the method further uses a covariance matrix calculated from simulated events accounting for the statistical and systematic uncertainties on the measurement as an input quantity. The method also requires the construction of a response matrix describing the detector smearing and reconstruction efficiency.

The output of the method includes an unfolded differential cross section in true kinematics, a covariance matrix describing the total uncertainty on the unfolded result, and an additional smearing matrix that we refer to as A_c. The
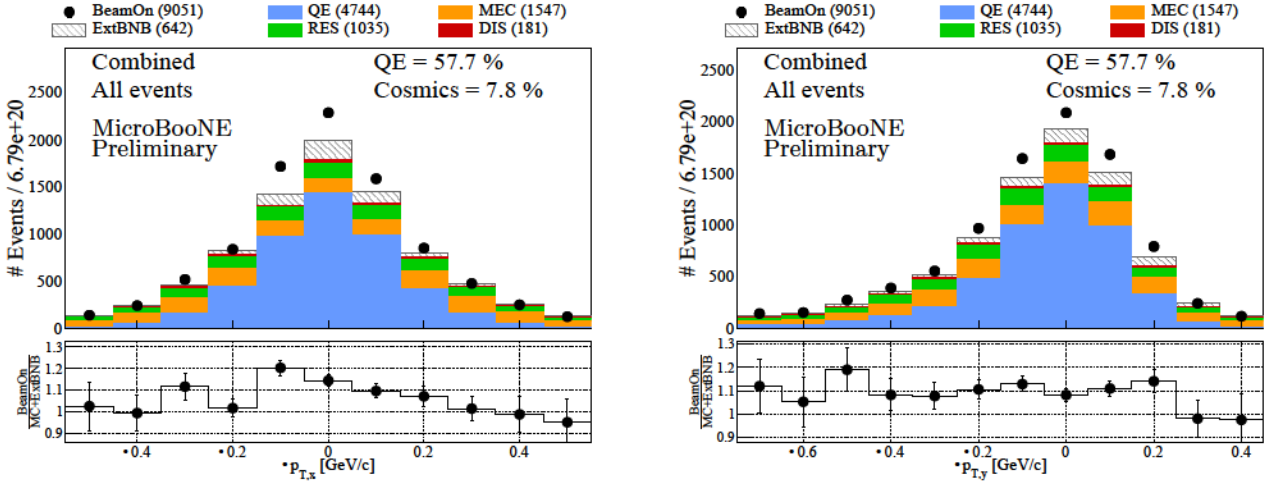
FIG. 2. Interaction breakdown of the CC1p0π events as a function of δp_{Tx} (left) and δp_{Ty} (right) into quasi-elastic (QE), meson exchange currents (MEC), resonance (RES), and deep inelastic scattering (DIS) events. ExtBNB refers to the cosmics acquired in the absence of the neutrino beam.

latter contains information about the regularization and bias of the measurement. The corresponding A_c matrices have been applied to the true cross section predictions included in this work when a comparison to the unfolded data is performed.

The required flux-averaged differential event rate $\tilde{\sigma}_{x,i}$ as a function of a given variable x is obtained by

$$\tilde{\sigma}_{x,i} = \frac{M_i - B_i}{N \cdot \Phi_\nu} \tag{5}$$

where M_i and B_i are the number of measured events and the expected background events, respectively. N is the number of target nucleons in the fiducial volume of interest. Φ_ν corresponds to the total BNB flux, which remains fixed so that the shape and normalization flux uncertainties are addressed in a correlated way [43].

The total covariance matrix $E_{ij} = E_{ij}^{stat} + E_{ij}^{syst}$ includes the statistical and systematic uncertainties on $\tilde{\sigma}$ associated with our measurement. E_{ij}^{stat} is a diagonal covariance matrix including the statistical uncertainties and E_{ij}^{syst} is a covariance matrix incorporating the total systematic uncertainties.

The neutrino flux is predicted using the flux simulation of the MiniBooNE Collaboration that used the same beam line [14]. Neutrino cross section modeling uncertainties were estimated using the GENIE framework of event reweighting [32, 33]. For both cross section and flux systematics, we use a multisim technique [44], which consists of generating many MC replicas, each one called a "universe", where model parameters are varied within their uncertainties. Each universe represents a different reweighting. The simultaneous reweighting of all model parameters allows the correct treatment of their correlations. A total of $k = 100$ such universes are used to construct a covariance matrix,

$$E_{ij} = \frac{1}{k} \sum_{n=1}^{n=k} (\tilde{\sigma}_i^n - \tilde{\sigma}_i^{CV}) \cdot (\tilde{\sigma}_j^n - \tilde{\sigma}_j^{CV}) \tag{6}$$

where $\tilde{\sigma}_i^{CV}$ ($\tilde{\sigma}_j^{CV}$) and $\tilde{\sigma}_i^n$ ($\tilde{\sigma}_j^n$) are the flux-averaged event rates for the central value and systematic universe k in a measured bin i(j) respectively.

A different approach is followed for detector model systematic uncertainties. In this case, one detector parameter is varied each time by 1σ and is referred to as a "unisim". These include variations in the light yield, the ionization electron recombination model, space-charge effects, and waveform deconvolution [45]. We then examined the impact of each parameter variation on the MC event rates by obtaining the differences with respect to the central value on a bin-by-bin basis. We defined the total detector 1σ systematic uncertainty by summing in quadrature the effect of m detector variations using the formalism introduced in Eqn. 6,

$$E_{ij} = \sum_{n=1}^{n=m} (\tilde{\sigma}_i^n - \tilde{\sigma}_i^{CV}) \cdot (\tilde{\sigma}_j^n - \tilde{\sigma}_j^{CV}). \tag{7}$$

An additional study using NuWro as fake data has been performed. The reconstructed NuWro signal events are propagated through the unfolding machinery and are compared to the truth-level cross section. The remaining difference between the unfolded and the true results normalized to $\sqrt{12}$ is assigned as the unfolding model uncertainty.

The statistical uncertainty of our measurement is 1.5%. The total uncertainty sums to 11% and includes contributions from the neutrino flux prediction (7.3%), neutrino interaction cross section modeling (5%), detector response modeling (4.9%), POT estimation (2.3%), number-of-scattering-targets (1.15%), reinteractions (1%), the unfolding model uncertainty (0.5%), and out-of-cryostat interaction modeling (0.2%).

Statistical uncertainties are shown with the inner error bars on the final results. The systematic uncertainties were decomposed into shape- and normalization-related sources following the approach outlined in [46]. The outer error bars on the reported cross sections correspond to statistical and shape uncertainties added in quadrature. The normalization uncertainties are presented with the gray band at the bottom of our results. The binning choice is driven by the demand that the statistical and the shape uncertainties are of comparable size in each bin.

SINGLE- AND DOUBLE-DIFFERENTIAL CROSS SECTIONS

The single- and double-differential cross sections as a function of δp_T are presented in Fig. 3. They are compared with G18 and the theory-driven GiBUU 2021 (GiBUU) event generator. Additional comparisons to the corresponding event generators when FSI are turned off were also included (G18 No FSI and GiBUU No FSI). G18 uses the Local Fermi Gas (LFG) model [47], the Nieves CCQE scattering prescription [48] which includes Coulomb corrections for the outgoing muon [49] and Random Phase Approximation (RPA) correction [50], the Nieves MEC model [51], the KLN-BS RES [52–55] and Berger-Sehgal COH [56] scattering models, the hA2018 FSI model [57], and MicroBooNE-specific tuning of model parameters [35]. GiBUU uses somewhat similar models, but, unlike GENIE, those are implemented in a coherent way, by solving the Boltzmann-Uehling-Uhlenbeck transport equation [58]. The modeling includes the Local Fermi Gas model [47], a standard CCQE expression [59], an empirical MEC model and a dedicated spin dependent resonances amplitude calculation following the MAID analysis [60]. The DIS model is as in PYTHIA [61] and the FSI treatment is different as the hadrons propagate through the residual nucleus in a nuclear potential which is consistent with the initial state.
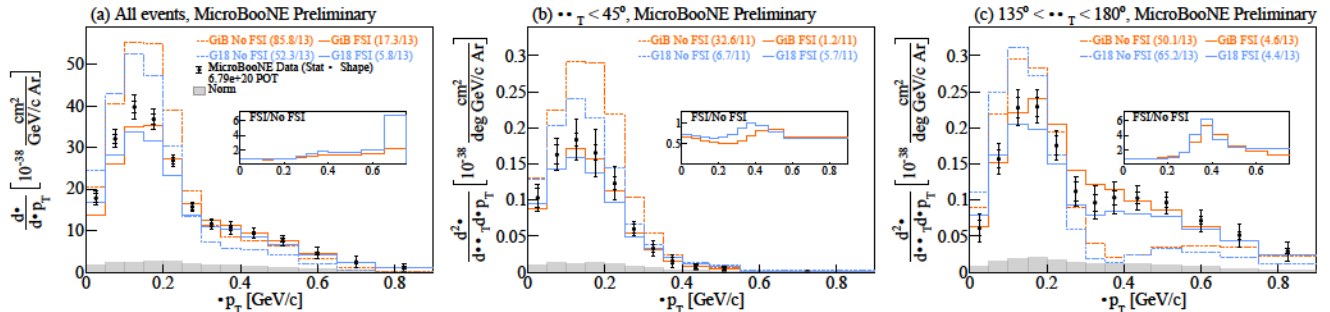

FIG. 3. The flux-integrated single- (a) and double- in $\delta\alpha_T$ bins (b and c) differential CC1p0π cross sections as a function of the transverse missing momentum δp_T. Inner and outer error bars show the statistical and total (statistical and shape systematic) uncertainty at the 1σ, or 68%, confidence level. The gray band shows the normalization systematic uncertainty. Colored lines show the results of theoretical absolute cross section calculations with and without FSI based on the GENIE and GiBUU event generators.

The single-differential results as a function of δp_T using all the events that satisfy our selection are shown in Fig. 3a. The peak height of both generator predictions is $\approx 30\%$ higher when FSI effects are turned off. Yet, all distributions illustrate a transverse missing momentum tail that extends beyond the Fermi momentum whether FSI effects are activated or not. The ratio between the generator predictions with and without FSI is shown in the insert and illustrates significant shape variations across the range of interest. The double-differential result shown in Fig. 3b using events with $\delta\alpha_T < 45^o$ is dominated by events that primarily occupy the region up to the Fermi momentum and do not exhibit a high momentum tail. The corresponding ratio insert illustrates a fairly uniform behavior indicative of transparency effects ranging between 50-70% in the region up to $\approx 300\,\mathrm{MeV/c}$. The double-differential results using events with $135^o < \delta\alpha_T < 180^o$ is shown in Fig. 3c and illustrate the high transverse missing momentum up to $1\,\mathrm{GeV/c}$. The case without FSI effects is strongly disfavored and the ratio insert illustrates strong shape variations.

Therefore, the high δp_T region is an appealing candidate for neutrino experiments to benchmark and tune the FSI modeling in event generators.

Apart from the nominal G18 prediction, we further performed a comparison to the recently added theory driven GENIE v3.0.6 G21_11b_00_000 configuration (G21 hN) [62]. The latter uses the SuSAv2 model for QE and MEC interactions [63], and the hN2018 FSI model [64]. The modeling options for RES, DIS, and COH interactions are the same as for G18. We investigated the effect of the FSI modeling choice by comparing the G21hN results to the ones obtained with G21 hA, where the hA2018 FSI model was used instead, and to G21 G4 with the recently coupled Geant4 FSI framework [65].
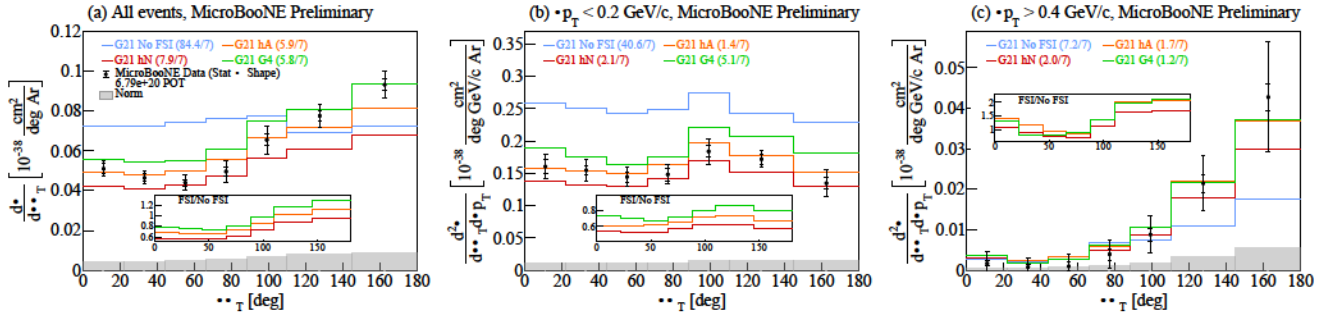

FIG. 4. The flux-integrated single- (a) and double- in δp_T bins (b and c) differential CC1p0π cross sections as a function of the angle $\delta\alpha_T$. Inner and outer error bars show the statistical and total (statistical and shape systematic) uncertainty at the 1σ, or 68%, confidence level. The gray band shows the normalization systematic uncertainty. Colored lines show the results of theoretical absolute cross section calculations with a number of FSI modeling options based on the GENIE event generator.

The single-differential results as a function of $\delta\alpha_T$ using all the events that satisfy our selection are shown in Fig. 4a. The result without FSI illustrates a uniform behavior across the whole distribution and is disfavored. The addition of FSI effects leads to a $\approx$ 30% asymmetry around $\delta\alpha_T = 90^o$ due to the fact that the selected proton undergoes FSI. The three FSI models used here for comparison result in a comparable performance, also shown in terms of the ratio plot of the different FSI options to the prediction without FSI. The double-differential result using events with $\delta p_T < 0.2$ GeV/c shown in Fig. 4b illustrates a uniform distribution indicative of the suppressed FSI impact in that part of the phase-space. The difference in the absolute scale between the No FSI result and the other predictions originates from the generation of events in the latter samples with multiple particles above detection threshold due to FSI effects. Such events do not satisfy the signal definition and are ignored and therefore introduce the difference in the absolute scale. The double-differential results using events with $\delta p_T > 0.4$ GeV/c is shown in Fig. 4c and illustrates the presence of strong FSI effects with a significantly enhanced asymmetry around 90°. Thus, the high $\delta\alpha_T$ region is the ideal candidate to test the FSI modeling performance in event generators.
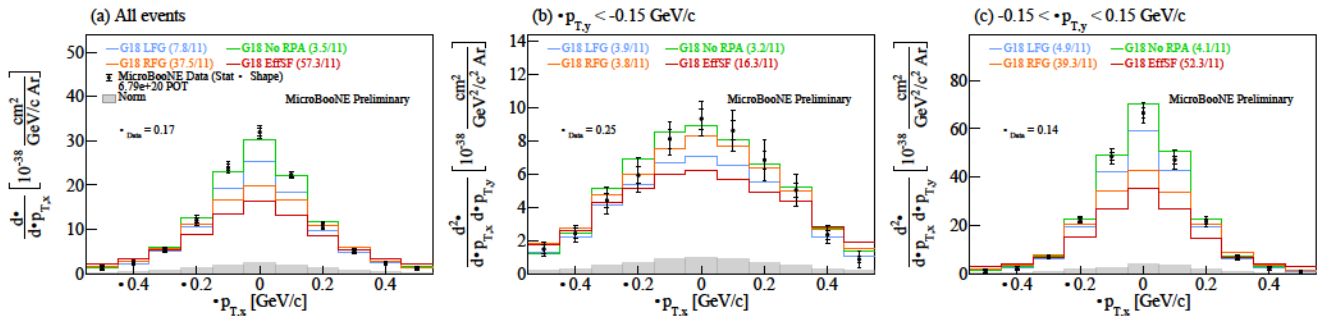

FIG. 5. The flux-integrated single- (a) and double- in $\delta p_{T,y}$ bins (b and c) differential CC1p0π cross sections as a function of the angle $\delta p_{T,x}$. Inner and outer error bars show the statistical and total (statistical and shape systematic) uncertainty at the 1σ, or 68%, confidence level. The gray band shows the normalization systematic uncertainty. Colored lines show the results of theoretical absolute cross section calculations with a number of event generators. The data standard deviation (σ) to a gaussian fit is shown.

Lastly, Fig. 5 shows the single- and double-differential results as a function of $\delta p_{T,x}$. The result shows the comparison between the nominal G18 LFG model and predictions using the same G18 modeling configuration but different nuclear

model options available in the GENIE event generator, namely the Bodek-Ritchie Fermi Gas (G18 RFG) [66] and an Effective Spectral Function (G18 EffSF) [67]. Furthermore, the prediction without Random Phase Approximation (RPA) effects is shown for comparison (G18 No RPA) [50].

The single differential result (Fig. 5a) illustrates a fairly broad symmetric distribution centered around 0. The double-differential result for events where $\delta p_{T,y} < -0.15$ GeV/c (Fig. 5b) illustrates an even broader distribution where all predictions yield comparable results, as can be seen in the data standard deviation (σ) reported on the figure. Unlike the asymmetric part of the $\delta p_{T,y}$ tail, the double-differential result for events with $-0.15 < \delta p_{T,y} < 0.15$ GeV/c (Fig. 5c) shows a much narrower peak which strongly depends on the choice of the underlying model and the addition or not of nuclear effects, such as RPA ones. The G18 LFG and G18 No RPA predictions are favored in that part of the phase-space.

The χ^2 per degree of freedom (d.o.f.) data comparison for each generator shown on all the results takes into account the total covariance matrix including the off-diagonal elements.

SUMMARY

We report the first measurement of ν_μ CC1p0π multi-differential cross sections on argon as a function of kinematic imbalance variables for event topologies with a single muon and a single proton detected in the final state. We compare our unfolded data results to a number of event generators, available model configurations and FSI modeling options. This measurement identifies regions of the phase-space which are ideal to provide constrains for nuclear effects in generator predictions essential for the extraction of oscillation parameters and highlights kinematic regimes where improvement of theoretical models is required.

[1] M. Tanabashi et al. Review of particle physics. *Phys. Rev. D*, 98:030001, Aug 2018.

[2] K. Abe et al. Constraint on the matter–antimatter symmetry-violating phase in neutrino oscillations. *Nature*, 580:339, 2020.

[3] B. Abi et al. The DUNE Far Detector Interim Design Report Volume 1: Physics, Technology and Strategies. *arXiv 1807.10334*, 2018.

[4] B. Abi et al. The DUNE Far Detector Interim Design Report Volume 2: Single-Phase Module. *arXiv*, 2018.

[5] B. Abi et al. The DUNE Far Detector Interim Design Report Volume 3: Dual-phasemodule. *arXiv*, 2018.

[6] M. Antonello et al. A Proposal for a Three Detector Short-Baseline Neutrino Oscillation Program in the Fermilab Booster Neutrino Beam. *arXiv*, 3 2015.

[7] P. Coloma and P. Huber. Impact of nuclear effects on the extraction of neutrino oscillation parameters. *Phys. Rev. Lett.*, 111:221802, Nov 2013.

[8] X.-G. et al Lu. Measurement of final-state correlations in neutrino muon-proton mesonless production on hydrocarbon at e=3gev. *Phys. Rev. Lett.*, 121:022504, Jul 2018.

[9] K. et al Abe. First t2k measurement of transverse kinematic imbalance in the muon-neutrino charged-current single-π^+ production channel containing at least one proton. *Phys. Rev. D*, 103:112009, Jun 2021.

[10] Andrew P. Furmanski and Jan T. Sobczyk. Neutrino energy reconstruction from one-muon and one-proton events. *Phys. Rev. C*, 95:065501, Jun 2017.

[11] J.A. Formaggio and G.P. Zeller. From eV to EeV: Neutrino Cross Sections Across Energy Scales. *Rev. Mod. Phys.*, 84:1307–1341, 2012.

[12] C. Anderson et al. First Measurements of Inclusive Muon Neutrino Charged Current Differential Cross Sections on Argon. *Phys. Rev. Lett.*, 108(10):161802, 2012.

[13] Y. Nakajima et al. Measurement of Inclusive Charged Current Interactions on Carbon in a Few-GeV Neutrino Beam. *Phys. Rev. D*, 83:012005, 2011.

[14] A.A. Aguilar-Arevalo et al. First measurement of the muon antineutrino double-differential charged-current quasielastic cross section. *Phys. Rev. D*, 88(3):032001, 2013.

[15] K. Abe et al. Measurement of the ν_μ charged-current quasielastic cross section on carbon with the ND280 detector at T2K. *Phys. Rev. D*, 92(11):112003, 2015.

[16] M.F. Carneiro et al. High-Statistics Measurement of Neutrino Quasielastic-Like Scattering at $E_\nu \sim 6$ GeV on a Hydrocarbon Target. *Phys. Rev. Lett.*, 124(12):121801, 2020.

[17] P. Abratenko et al. First Measurement of Inclusive Muon Neutrino Charged Current Differential Cross Sections on Argon at $E_\nu \sim 0.8$ GeV with the MicroBooNE Detector. *Phys. Rev. Lett.*, 123(13):131801, 2019.

[18] G.A. Fiorentini et al. Measurement of Muon Neutrino Quasielastic Scattering on a Hydrocarbon Target at $E_\nu \sim 3.5$ GeV. *Phys. Rev. Lett.*, 111:022502, 2013.

[19] M. Betancourt et al. Direct Measurement of Nuclear Dependence of Charged Current Quasielasticlike Neutrino Interactions Using MINERνA. *Phys. Rev. Lett.*, 119(8):082001, 2017.

[20] T. Walton et al. Measurement of muon plus proton final states in ν_μ interactions on hydrocarbon at $\langle E_\nu \rangle = 4.2$ GeV. *Phys. Rev. D*, 91(7):071301, 2015.

[21] K. Abe et al. Characterization of nuclear effects in muon-neutrino scattering on hydrocarbon with a measurement of final-state kinematics and correlations in charged-current pionless interactions at T2K. *Phys. Rev. D*, 98(3):032003, 2018.

[22] P. Abratenko et al. First measurement of differential charged current quasielasticlike ν_μ-argon scattering cross sections with the microboone detector. *Phys. Rev. Lett.*, 125:201803, Nov 2020.

[23] R. Acciarri et al. Design and Construction of the MicroBooNE Detector. *J. Instrum.*, 12(02):P02017, 2017.

[24] F. Tortorici, V. Bellini, and C.M. Sutera. Upgrade of the ICARUS T600 Time Projection Chamber. *J. Phys. Conf. Ser.*, 1056(1):012057, 2018.

[25] R. Acciarri et al. The Pandora multi-algorithm approach to automated pattern recognition of cosmic-ray muon and neutrino events in the MicroBooNE detector. *Eur. Phys. J. C*, 78(1):82, 2018.

[26] M.J. Berger, J.S. Coursey, M.A. Zucker, and J. Chang. Stopping powers and ranges for protons and alpha particles. NIST Standard Reference Database 124, 2017.

[27] P. Abratenko et al. Cosmic ray background rejection with wire-cell lartpc event reconstruction in the microboone detector. *Phys. Rev. Applied*, 15:064071, Jun 2021.

[28] D. Kaleko et al. PMT Triggering and Readout for the MicroBooNE Experiment. *J. Instrum.*, 8:C09009, 2013.

[29] C. Adams et al. Ionization electron signal processing in single phase LArTPCs. Part II. Data/simulation comparison and performance in MicroBooNE. *J. Instrum.*, 13(07):P07007, 2018.

[30] Wouter Van De Pontseele. *Search for Electron Neutrino Anomalies with the MicroBooNE Detector*. PhD thesis, Oxford U., 2020.

[31] P. Abratenko et al. Calorimetric classification of track-like signatures in liquid argon TPCs using MicroBooNE data. *JHEP*, 153, 202.

[32] C. Andreopoulos et al. The GENIE Neutrino Monte Carlo Generator. *Nucl. Instrum. Meth. A*, 614:87–104, 2010.

[33] C. Andreopoulos et al. The GENIE Neutrino Monte Carlo Generator: Physics and User Manual. *arXiv*, 10 2015.

[34] K. Abe et al. Measurement of double-differential muon neutrino charged-current interactions on c8h8 without pions in the final state using the t2k off-axis beam. *Phys. Rev. D*, 93:112012, Jun 2016.

[35] P. Abratenko et al. New CC0π genie model tune for microboone. *Phys. Rev. D*, 105:072001, Apr 2022.

[36] S. Agostinelli et al. Geant4-a simulation toolkit. *Nucl. Instrum. Meth.*, A 506, 2003.

[37] R. Pordes and E. Snider. The Liquid Argon Software Toolkit (LArSoft): Goals, Status and Plan. *PoS*, ICHEP2016:182, 2016.

[38] E. Snider and G. Petrillo. LArSoft: Toolkit for Simulation, Reconstruction and Analysis of Liquid Argon TPC Neutrino Detectors. *J. Phys. Conf. Ser.*, 898(4):042057, 2017.

[39] C. Adams et al. Ionization electron signal processing in single phase LArTPCs. part i. algorithm description and quantitative evaluation with MicroBooNE simulation. *Journal of Instrumentation*, 13(07):P07006–P07006, jul 2018.

[40] Tomasz Golan, Cezary Juszczak, and Jan T. Sobczyk. Effects of final-state interactions in neutrino-nucleus interactions. *Phys. Rev. C*, 86:015505, Jul 2012.

[41] T. et al Cai. Nucleon binding energy and transverse momentum imbalance in neutrino-nucleus reactions. *Phys. Rev. D*, 101:092001, May 2020.

[42] W. Tang, X. Li, X. Qian, H. Wei, and C. Zhang. Data unfolding with wiener-svd method. *Journal of Instrumentation*, 12(10):P10002–P10002, Oct 2017.

[43] Lukas Koch and Stephen Dolan. Treatment of flux shape uncertainties in unfolded, flux-averaged neutrino cross-section measurements. *Phys. Rev. D*, 102:113012, Dec 2020.

[44] B.P. Roe. Statistical errors in Monte Carlo estimates of systematic errors. *Nucl. Instrum. Meth. A*, 570:159–164, 2007.

[45] MicroBooNE Collaboration. Novel approach for evaluating detector-related uncertainties in a lartpc using microboone data. *EPJC 82, Article number: 454*, 2022.

[46] Kendall Mahn. *A search for muon neutrino and antineutrino disappearance in the Booster Neutrino Beam*. PhD thesis, Columbia University, 2009.

[47] R.C. Carrasco and E. Oset. Interaction of Real Photons With Nuclei From 100-MeV to 500-MeV. *Nucl. Phys. A*, 536:445–508, 1992.

[48] J. Nieves, F. Sanchez, I. Ruiz Simo, and M.J. Vicente Vacas. Neutrino Energy Reconstruction and the Shape of the CCQE-like Total Cross Section. *Phys. Rev. D*, 85:113008, 2012.

[49] Jonathan Engel. Approximate treatment of lepton distortion in charged current neutrino scattering from nuclei. *Phys. Rev. C*, 57:2004–2009, 1998.

[50] J. Nieves, J. E. Amaro, and M. Valverde. Inclusive quasielastic charged-current neutrino-nucleus reactions. *Phys. Rev. C*, 70:055503, Nov 2004.

[51] J. Schwehr, D. Cherdack, and R. Gran. GENIE implementation of IFIC Valencia model for QE-like 2p2h neutrino-nucleus cross section. *arXiv 1601.02038*, 2016.

[52] J. A. Nowak. Four Momentum Transfer Discrepancy in the Charged Current π^+ Production in the MiniBooNE: Data vs. Theory. *AIP Conf. Proc.*, 1189(1):243–248, 2009.

[53] K. Kuzmin et al. Lepton polarization in neutrino nucleon interactions. *Phys. Part. Nucl.*, 35:S133–S138, 2004.

[54] Ch. Berger and L.M. Sehgal. Lepton mass effects in single pion production by neutrinos. *Phys. Rev. D*, 76:113004, 2007.

[55] K. M. Graczyk and J. T. Sobczyk. Form Factors in the Quark Resonance Model. *Phys. Rev. D*, 77:053001, 2008. [Erratum: Phys.Rev.D 79, 079903 (2009)].

[56] C. Berger and L. Sehgal. PCAC and coherent pion production by low energy neutrinos. *Phys. Rev. D*, 79:053003, 2009.

[57] D. Ashery, I. Navon, G. Azuelos, H.K. Walter, H.J. Pfeiffer, and F.W. Schleputz. True Absorption and Scattering of Pions on Nuclei. *Phys. Rev. C*, 23:2173–2185, 1981.

[58] U. Mosel. Neutrino event generators: foundation, status and future. *Phys. Rev. G*, 2019.

[59] Tina Leitner, L. Alvarez-Ruso, and U. Mosel. Charged current neutrino nucleus interactions at intermediate energies. *Phys. Rev. C*, 73:065502, 2006.

[60] Ulrich Mosel. Neutrino event generators: foundation, status and future. *J. Phys. G*, 46(11):113001, 2019.

[61] Torbjorn Sjostrand, Stephen Mrenna, and Peter Z. Skands. PYTHIA 6.4 Physics and Manual. *JHEP*, 05:026, 2006.

[62] GENIE Collaboration. Recent highlights from genie v3. *Eur. Phys. J. Spec. Top.*, 2021.

[63] S. Dolan, G. D. Megias, and S. Bolognesi. Implementation of the susav2-meson exchange current 1p1h and 2p2h models in genie and analysis of nuclear effects in t2k measurements. *Phys. Rev. D*, 101:033003, Feb 2020.

[64] L. A. Harewood and R. Gran. Elastic hadron-nucleus scattering in neutrino-nucleus reactions and transverse kinematics measurements. *arXiv:1906.10576*, 2019.

[65] D. H. Wright and M. H. Kelsey. The Geant4 Bertini Cascade. *Nucl. Instrum. Meth. A*, 804:175–188, 2015.

[66] A. Bodek and J. L. Ritchie. Fermi-motion effects in deep-inelastic lepton scattering from nuclear targets. *Phys. Rev. D*, 23:1070–1091, Mar 1981.

[67] Artur M. Ankowski and Jan T. Sobczyk. Argon spectral function and neutrino interactions. *Phys. Rev. C*, 74:054316, Nov 2006.